DE GRUYTER Nanophotonics 2025; 14(23): 4099–4112

Research Article

Michele Cotrufo, Domenico de Ceglia, Hyunseung Jung, Igal Brener, Dragomir Neshev, Costantino De Angelis and Andrea Alù*

Nonlinear analog processing with anisotropic nonlinear films

https://doi.org/10.1515/nanoph-2024-0770
Received December 24, 2024; accepted May 11, 2025;

Abstract: Digital signal processing is the cornerstone of several modern-day technologies, yet in multiple applications it faces critical bottlenecks related to memory and speed constraints. Thanks to recent advances in metasurface design and fabrication, light-based analog computing has emerged as a viable option to partially replace or augment digital approaches. Several light-based analog computing functionalities have been demonstrated using patterned flat optical elements, with great opportunities for integration in compact nanophotonic systems. So far, however, the available operations have been restricted to the linear regime, limiting the impact of this technology to a compactification of Fourier optics systems. In this paper, we introduce nonlinear operations to the field of metasurface-based analog optical processing, demonstrating that nonlinear optical phenomena, combined with nonlocality in flat optics, can be leveraged to synthesize kernels beyond linear Fourier optics, paving the way to a broad range of new opportunities. As a practical demonstration, we report the experimental synthesis of a class of nonlinear operations that can be used to realize broadband, polarization-selective analog-domain edge detection.

Keywords: metasurfaces; nonlinear; analog image processing

1 Introduction

Prof. Federico Capasso is broadly considered the pioneer and father of flatland optics. Such flat-optics devices exhibiting a linear and local (LL) response can be generally defined by a spatially varying linear transfer function $T_{\mathrm{LL}}(\mathbf{r})$, which depends on the position $\mathbf{r}$, and which can be locally tailored through meta-atoms spatially arranged to form metasurfaces (Figure 1a). An input signal, defined in real space by a complex electric field amplitude $E_{\mathrm{in}}^{\omega}(\mathbf{r})$, is filtered linearly and locally and transformed into an output field $E_{\mathrm{out}}^{\omega}(\mathbf{r}) = T_{\mathrm{LL}}(\mathbf{r})E_{\mathrm{in}}^{\omega}(\mathbf{r})$. Wavefront engineering is arguably the most prominent application of LL systems: anomalous reflection and refraction for beam steering, focusing and holography have been implemented in a variety of metasurfaces, within plasmonic and dielectric platforms, and in either resonant or nonresonant systems [1]. Spatial dispersion, i.e., nonlocality induced by the long-range coupling of multiple unit cells, is usually treated as a nuisance in LL flat-optics devices, since it complicates their design. However, the nonlocal response of metasurfaces has recently emerged as an additional degree of freedom to achieve advanced functionalities, based on the independent control over spectral and angular selectivity [2]. Nonlocality is usually achieved in patterned flat-optics structures by engineering spatially delocalized resonances, such as guided-mode-resonance gratings and quasi-bound states in the continuum [3]. To date, however, investigations into engineered nonlocalities in metasurfaces have primarily focused on the linear-optics regime. The action of linear nonlocal (LN) systems is well described by a k-dependent transfer function $T_{\mathrm{LN}}(\mathbf{k})$, which defines how the metasurface filters the

---

Michele Cotrufo and Domenico de Ceglia contributed equally to this work.

***Corresponding author: Andrea Alù**, Photonics Initiative, Advanced Science Research Center, City University of New York, New York, NY 10031, USA; and Physics Program, Graduate Center of the City University of New York, New York, NY 10016, USA, E-mail: aalu@gc.cuny.edu. https://orcid.org/0000-0002-4297-5274

Michele Cotrufo, Photonics Initiative, Advanced Science Research Center, City University of New York, New York, NY 10031, USA; and The Institute of Optics, University of Rochester, Rochester, NY 14627, USA. https://orcid.org/0000-0001-9931-1279

Domenico de Ceglia and Costantino De Angelis, CNIT and Department of Information Engineering, University of Brescia, Via Branze, 38, Brescia, 25123, Italy; and Istituto Nazionale di Ottica, Consiglio Nazionale delle Ricerche, Via Branze, 45, Brescia, 25123, Italy

Hyunseung Jung and Igal Brener, Center for Integrated Nanotechnologies, Sandia National Laboratories, POB 5800, Albuquerque, NM 87185, USA, E-mail: ibrener@sandia.gov (I. Brener). https://orcid.org/0000-0002-2139-5182 (I. Brener)

Dragomir Neshev, ARC Centre of Excellence for Transformative Meta-Optical Systems (TMOS), Research School of Physics, Australian National University, Canberra, Australia. https://orcid.org/0000-0002-4508-8646

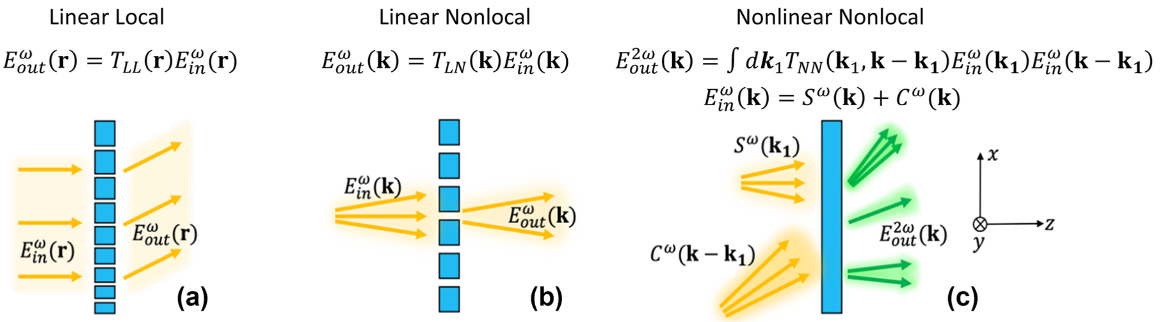

Figure 1: Comparison between transfer functions of flat optical elements with LL, LN, and NN responses, and typical operations of the three systems. (a) Beam deflection obtained in a linear and local (LL) system. (b) Passive filtering of spatial frequencies obtained in a linear and nonlocal (LN) system. (c) A nonlinear and nonlocal (NN) system allows nonlinear mixing of a signal field S^{ω} and a control field C^{ω}, enabling different kinds of nonlinear image processing.

angular spectrum $E^{\omega}_{\text{in}}(\mathbf{k})$ of the input function, according to $E^{\omega}_{\text{out}}(\mathbf{k}) = T_{\text{LN}}(\mathbf{k})E^{\omega}_{\text{in}}(\mathbf{k})$, as described in Figure 1b. This transfer function resembles the conventional working principle of Fourier optics systems [4]; hence, nonlocal metasurfaces have been recently exploited as a platform to compactify linear analog computing and image processing. For example, n-th order spatial differentiation [5] can be achieved by tailoring the nonlocality to produce transfer functions $T_{\text{LN}}(\mathbf{k}) \propto (i\mathbf{k})^{n}$, while integration is obtained by synthesizing transfer functions $T_{\text{LN}}(\mathbf{k}) \propto (i\mathbf{k})^{1/n}$. LN flat-optics elements readily accommodate image processing functionalities, such as edge detection [6]–[21] and blurring filters, via high-pass or low-pass spatial-frequency filtering. Despite their appealing features, linear metasurfaces – both local and nonlocal – face limitations related to the restricted numerical aperture and frequency bandwidth [14], [22], but most importantly to the inherent linearity of the mathematical operations that can be engineered. In fact, any image processing achieved by linear metasurfaces can be also achieved with bulk approaches, such as Fourier $4f$ lens systems. Efforts to overcome these constraints become crucial to push the boundaries of all-optical analog computing metasurfaces and enhancing their capabilities. For instance, deep learning and cryptography inherently require nonlinear functionalities, which cannot be achieved through Fourier optics. In this paper, we demonstrate that the combination of nonlinear and nonlocal effects in the same flat-optics device offers a powerful strategy to achieve advanced image processing and analog computing functionalities beyond the limits of Fourier systems, offering reduced structural complexity and increased efficiency in terms of angular and frequency bandwidth.

The concept of nonlinear nonlocal (NN) flat-optics is illustrated in Figure 1c, highlighting the differences with respect to LL and LN approaches. NN flat-optics elements stand out because they can induce nonlinear mixing of spatial and/or temporal frequencies of the input signals. Consider, for example, a scenario in which two fields, a *signal* field $S^{\omega}(\mathbf{r})$ and a *control* field $C^{\omega}(\mathbf{r})$, impinge on a NN flat-optics with a large second-order nonlinear response. We denote with $S^{\omega}(\mathbf{k})$ and $C^{\omega}(\mathbf{k})$ the angular spectrum decompositions of these fields and, for simplicity, we focus here on the case in which these two fields have the same frequency. The second-harmonic field generated by the total input field, $E^{\omega}_{\text{in}}(\mathbf{k}) = S^{\omega}(\mathbf{k}) + C^{\omega}(\mathbf{k})$, can be described by a bi-dimensional transfer function $T_{\text{NN}}(\mathbf{k}, \mathbf{k}')$, i.e., $E^{2\omega}_{\text{out}}(\mathbf{k}) = \int d\mathbf{k}_1 T_{\text{NN}}(\mathbf{k}_1, \mathbf{k}-\mathbf{k}_1)E^{\omega}_{\text{in}}(\mathbf{k}_1)E^{\omega}_{\text{in}}(\mathbf{k}-\mathbf{k}_1)$ (Figure 1c). Thus, the angular decomposition of the output field, $E^{2\omega}_{\text{out}}(\mathbf{k})$, is given by the combination of different contributions involving the bi-dimensional transfer function and the signal and control fields. As a result, the output field contains self-mixing and cross-mixing terms of the input spatial frequencies. By gaining control over the transfer function $T_{\text{NN}}(\mathbf{k}, \mathbf{k}')$, nonlinear image processing functionalities can be unlocked. Based on the recent progress in engineering nonlocalities over metasurfaces, it appears that flat optics can form an excellent platform for tailoring the NN transfer functions [23]. Quite remarkably, as we show in the following, even unpatterned thin films can display a nontrivial NN response sufficient to bestow nonlinear image processing capabilities, provided that the nonlinear material of the film supports specific asymmetries [24]. Such functionality can be dynamically controlled through the control signal, unlocking not only nonlinear image processing operations but also broad reconfigurability, which is not straightforward in linear metasurfaces. In addition, unpatterned thin films featuring nonlinear nonlocality can feature bandwidth and NA much larger than their linear counterparts, offering an exciting platform that can be further augmented by structuring the films in space. While nonlinear computations based on nonlinear unpatterned films are expected to have an inherently low power efficiency (as nonlinear optical processes in thin films are very weak), this issue can be overcome by inducing low-quality-factor modes into our flat-optic devices, which could provide a large resonant enhancement (and thus a power efficiency boost) without compromising the fidelity of the mathematical operation.

2 Results

2.1 Unpatterned flat optics with NN response

To elucidate the potential of combining nonlinearity and nonlocality, we discuss the basic scenario of a nonlinear thin anisotropic film for analog image processing [24]. The geometry in Figure 2 refers to an unpatterned thin film made of a material with second-order nonlinear susceptibility, sufficiently large that we can neglect higher-order nonlinear processes. We consider a two-dimensional problem, with translational invariance of the fields and optical properties along the y direction. In addition, we assume that the nonlinear film has a thickness t smaller than the wavelength of the excitation fields $\left(t \ll \lambda_0\right)$ and it is located at $z = 0$, so that the system can be approximated by a 2D sheet. The nonlinear response of such thin film is mainly dictated by the structure of the second-order nonlinear susceptibility tensor $\chi^{(2)}$, and thus by the chosen material and its crystallographic orientation. Previous works [24] have considered materials for which the only nonzero component of the $\chi^{(2)}$ tensor is $\chi^{(2)}_{zzz}$. Here, we consider a broader and more realistic class of materials, characterized by a nonlinear susceptibility tensor for which only the elements $\chi^{(2)}_{ijk}$ with $i \neq j \neq k$ are nonzero. This is the case of zincblende-type crystals, like gallium arsenide (GaAs) (assuming that the Cartesian axis are oriented along the [100], [010] and [001] axis of the crystal), a material platform with large quadratic nonlinearity that has garnered interest in the field of nonlinear photonics for the development of nonlinear metasurfaces for efficient harmonic generation [25]–[28]. The film is excited by two coherent fields with same frequency: a signal and a control field, both p-polarized (electric fields oscillating in the plane xz), so that the second-harmonic field is y-polarized. Hence, second-harmonic generation is mediated by the $\chi^{(2)}_{yxz}$ and $\chi^{(2)}_{yzx}$ elements of the nonlinear susceptibility tensor. In this illustrative example, the control field $C^{\omega}(\mathbf{r})$ takes the form of a Gaussian beam with a large diameter ($\gg \lambda_0$) impinging at oblique incidence with angle θ_c, imparting a linear phase profile across the flat-optics element. The signal field is a small-divergent and normally incident image modulated in amplitude along the x direction by an arbitrary function $s(x)$. For illustrative purposes, we consider a signal made by two adjacent Gaussian profiles. The signal and the control fields on the flat-optics element can be written as

$$S^{\omega}(\mathbf{r}) = \left[\hat{x}s(x)S^{\omega} + \hat{z}S^{\omega}_{z}\right]e^{-i\mathbf{k}_{\mathrm{S}}\cdot\mathbf{r}}, \tag{1}$$

$$C^{\omega}(\mathbf{r}) = \hat{\theta}_c C^{\omega}e^{-i\mathbf{k}_{\mathrm{C}}\cdot\mathbf{r}}, \tag{2}$$

where $\hat{\mathbf{k}}_{\mathbf{S}} = \hat{z}$, $\hat{\mathbf{k}}_{\mathbf{C}} \cdot \hat{x} = \sin\theta_C$, and $\hat{\theta}_c = \cos\theta_C\hat{x} - \sin\theta_C\hat{z}$. Importantly, the signal field carries a component along the longitudinal direction z, associated with the field gradients introduced by the spatial modulation $s(x)$. Indeed, by applying Gauss's law in the absence of charges [29], and adopting the small-divergence approximation ($k_z \approx k_0$), we find $S^{\omega}_{z} \approx -\frac{iS^{\omega}}{k_0}\frac{\partial s(x)}{\partial x}$. Thus, the z-component of the signal field is proportional to the first derivative of $s(x)$.

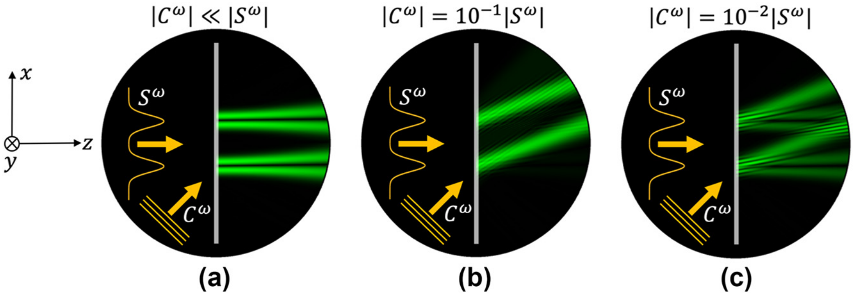

Figure 2: Functionalities of a nonlinear nonlocal (NN) flat-optics element made of a thin film of gallium arsenide. The system is illuminated by two coherent beams: a control (C) and a signal (S), reported in orange. (a) When the amplitude of the control is much smaller than the amplitude of the signal, nonlinear edge detection is performed at the SH (the green beam transmitted is the "edge" of the signal, i.e., it is proportional to the derivative of the signal). (b) When $|C^{\omega}| = 0.1|S^{\omega}|$, nonlinear beam deflection is dominant. (c) When $|C^{\omega}| = 0.1|S^{\omega}|$, the generated SH signal performs simultaneous nonlinear edge detection and nonlinear beam deflection of the signal. The deflection angle is determined by the angle of incidence of the control signal.

The nonlinear film mixes signal and control fields, resulting in a second-harmonic polarization current, in the plane $z = 0$, given by

$$\mathbf{P}^{2\omega} = 2\varepsilon_0 t \chi^{(2)}_{yxz}\left[s(x)S^{\omega} + \cos\theta_c C^{\omega} e^{-ik_0 \sin\theta_c x}\right] \times \left[S^{\omega}_z - \sin\theta_c C^{\omega} e^{-ik_0 \sin\theta_c x}\right]\hat{y}, \tag{3}$$

which in turn generates a y-polarized second-harmonic field $\mathbf{E}^{2\omega} = G_{yy}\mathbf{P}^{2\omega}$, where $G_{yy} = \frac{2\pi i}{\varepsilon_0 \lambda_0}$ is the Green's function of free space. The second-harmonic field contains four terms,

$$\begin{aligned}\mathbf{E}^{2\omega} = {} & \hat{y} 4\pi i \frac{t}{\lambda_0}\chi^{(2)}_{yxz}\left[s(x)S^{\omega}S^{\omega}_z + C^{\omega}S^{\omega}_z \cos\theta_c e^{-ik_0 \sin\theta_c x}\right.\\ & - s(x)S^{\omega}C^{\omega} \sin\theta_c e^{-ik_0 \sin\theta_c x} - \left(C^{\omega}\right)^2 \\ & \left.\times \sin\theta_c \cos\theta_c e^{-i2k_0 \sin\theta_c x}\right],\end{aligned} \tag{4}$$

which correspond to different nonlinear mixing products of the signal and control fields. Starting from this general result, we can now analyze different special scenarios: first, let us consider the case in which the control field is small or absent (i.e., $|C^{\omega}| \ll |S^{\omega}|$), as in Figure 2a. The first term in Eq. (4), proportional to $s(x)S^{\omega}S^{\omega}_z$, is dominant in this case, and it is the only one that emerges perpendicularly with respect to the film. The corresponding SHG field, emerging from the right side (green pattern), contains four peaks, corresponding to the points where the two input Gaussian peaks have the largest slopes. Since the SHG field amplitude is proportional to the signal gradients, this operation can be used to realize a nonlinear form of edge detection on the input function $s(x)$.

We emphasize that the edge detection obtained here (Figure 2a) is not only based on a different mathematical operation, nonlinear in nature, than in the case of Fourier optical elements, but it is also based on a fundamentally different phenomenon than the one obtained in linear metasurfaces [6]–[21]. Here, edge detection is obtained by exploiting the anisotropy of the $\chi^{(2)}$ tensor of GaAs and the corresponding polarization- and angle-selective response with respect to free-space radiations. In the case of GaAs, the SH field is proportional to the longitudinal component of the input field, which in turn carries information about the spatial derivative of the image. This is in contrast to linear approaches to edge detection, which rely on Fourier filtering performed by linear metasurfaces [3], [5], [12], [14], [19]. In those systems, a dispersive resonance is engineered in order to induce a strong variation of the linear transmission with angle of incidence, which then leads to a Laplacian-type operator in the Fourier domain. Because of this mechanism and the need for high-Q resonances, these linear devices are inherently narrowband. In contrast, the output SH field generated by the NN response of the thin GaAs film contains the product of the signal by its first derivative – a nonlinear operation, which cannot be obtained with any linear system. In addition, the approach demonstrated here (Eqs. (1)–(4)) does not require a resonance or tailored dispersion, and thus it inherently benefits from a broad operational spectral bandwidth. The bandwidth is only limited by the possible onset of absorption inside the thin layer for photons with energy above the material bandgap, as we report experimentally in the next section.

The second and third terms in Eq. (4) are cross-terms produced by the spatial-frequency mixing of control and signal fields. They form a beam that propagates in the direction $\theta_{CS} = \operatorname{asin}\left(\frac{\sin\theta_C}{2}\right)$. In the small divergence approximation $\left(k_z \approx k_0 \gg \left|\frac{\partial}{\partial x}\right|\right)$, the main contribution contained in this beam is the third term in Eq. (4), proportional to $-s(x)S^{\omega}C^{\omega} \sin\theta_c e^{-ik_0 \sin\theta_c x}$. This term is a scaled version of the input signal deflected toward θ_{CS}. Importantly, the deflection angle θ_{CS} is solely determined by the incident angle of the control signal, whereas the amplitude of the control signal may be tuned to make the beam-deflection effect dominant. For example, in Figure 2b, a nonlinear beam deflection can be clearly seen for $|C^{\omega}| = 0.1|S^{\omega}|$.

Another interesting scenario is displayed in Figure 2c for the case $|C^{\omega}| = 0.01|S^{\omega}|$. Here, the nonlinear edge-detection in the normal direction and the deflection of the input image at the angle θ_{CS} happen simultaneously. Such a regime may be of interest for applications where simultaneous access to the unprocessed and processed images is required. The fourth term in Eq. (4) is transversely phase-matched to the control plane wave, and therefore, it is the only one that emerges at the angle θ_C. This term is not particularly interesting, and it becomes dominant only when $|C^{\omega}| \gg |S^{\omega}|$.

The examples discussed in Figure 2 showcase various intriguing capabilities of NN systems, even in the most basic scenario of an unpatterned thin film: (i) image processing functionalities that typically require patterned metasurfaces in the linear regime, such as beam deflection (or anomalous refraction) and edge detection, may be achieved by leveraging the nonlinear and nonlocal response of unpatterned thin films; (ii) the response of an NN system is intensity and control-beam dependent, hence tunable – in the example above one can switch the functionality from beam defection to edge detection by varying the ratio of signal and control amplitudes; (iii) the resulting operations are inherently nonlinear – for instance, edge detection here is nonlinear and fundamentally different from the Laplacian produced by a linear optical system, as it results from the multiplication of two fields, specifically, the signal itself multiplied by its derivative; (iv) since this approach does not rely on a resonance, it is also free from fundamental constraints on the operational spectral bandwidth, as it happens instead for linear devices based on resonances or tailored dispersion; (v) more complex nonlinear functionalities may be realized by leveraging the control function as a means to write functionalities – while in the reported example, the control is only used to achieve nonlinear beam deflection, for more sophisticated functionalities, such as nonlinear holography, the control may be a structured beam with arbitrary amplitude and phase profile; (vi) by locally structuring the metasurface, we may induce engineered resonances that trade bandwidth for efficiency, and we may engineer the nonlocality of the $\chi^{(2)}$ tensor, opening the design space to more complex nonlinear operators.

2.2 Nonlinear edge detection in nonlinear unpatterned films

Edge detection with NN flat-optics has been theoretically proposed [24] based on a thin layer of nonlinear material with susceptibility tensor featuring only the $\chi^{(2)}_{zzz}$ element. This type of response can be achieved, for example, at interfaces [30], in nanolaminate films [31], and in quantum well systems [32]. Here, based on the general formalism described above, we demonstrate theoretically and experimentally that nonlinear edge detection is not limited to materials for which the nonlinear permittivity is dominated by $\chi^{(2)}_{zzz}$. By contrast, we show that broadband edge detection arises in unpatterned flat-optics with any type of nonlinear susceptibility tensor that involves at least one longitudinal component of the input pump field. Building upon the example outlined in the previous section, we consider a NN system comprising an unpatterned thin film of (001) GaAs (Figure 3a). For nonlinear edge detection (Figure 2a), the control signal is not necessary. To understand the mechanism of nonlinear edge detection in the GaAs flat-optics system, we assume that the input image, carried by a wave at the fundamental frequency (FF), is projected on the nonlinear film. Using the same approach outlined in the previous section, the FF pump can be written as: $\mathbf{E}^{\omega} = \mathbf{E}^{\omega}_{\perp} + E^{\omega}_{z}\hat{z}$, where the longitudinal component is $E^{\omega}_{z} \approx \frac{i}{k}\left(\frac{\partial E^{\omega}_{x}}{\partial x} + \frac{\partial E^{\omega}_{y}}{\partial y}\right)$ [29]. It follows that any nonlinear flat-optics system that is sensitive to E^{ω}_{z} – i.e., which can generate a nonlinear polarization when a z-polarized pump field is present – will produce a nonlinear signal proportional to the spatial derivative of the pump field. One of these systems is the unpatterned GaAs film considered here. Indeed, owing to

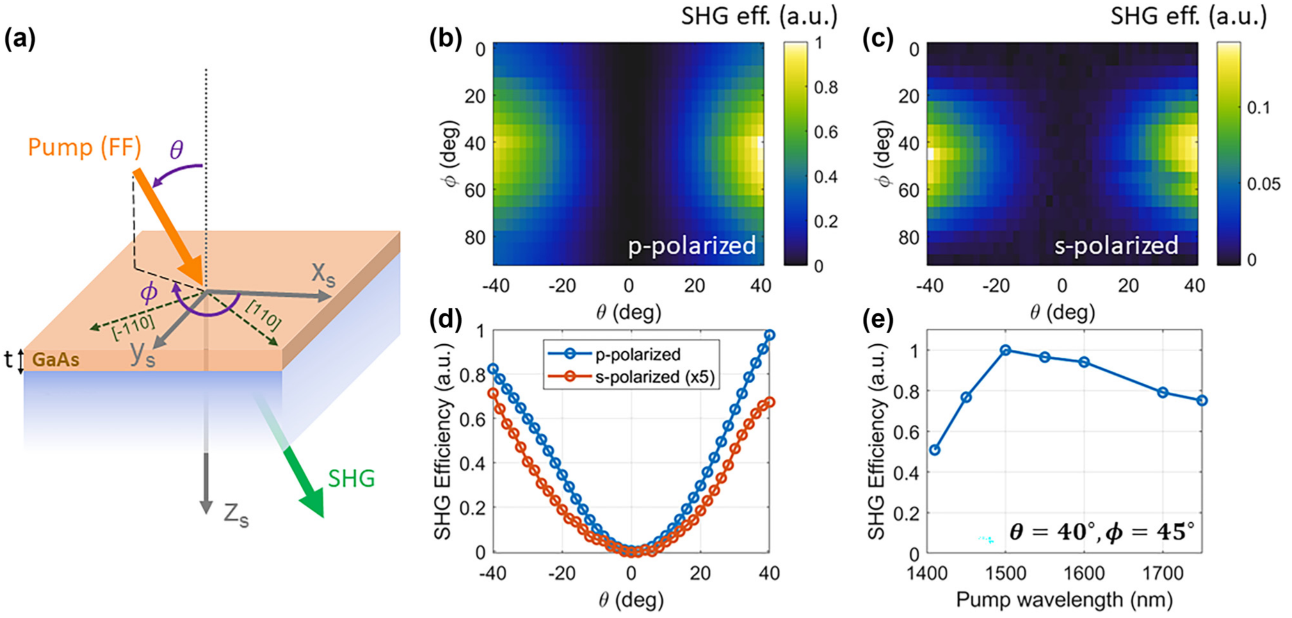

Figure 3: Sample and preliminary characterization. (a) Schematic of the sample and measurement. A thin layer of GaAs is bonded on a quartz substrate. The axes x_s, y_s, and z_s are aligned to the [100], [010], and [001] crystal directions of the sample, respectively. The sample is excited by a pump beam (orange arrow) at the fundamental frequency (FF) impinging along a direction defined by the polar (θ) and azimuthal (ϕ) angle, and with either s or p polarization. The second-harmonic emission (green arrow) generated along a direction parallel to the pump is collected on the opposite side of the sample. (b–c) Measured SHG efficiency (arbitrary units) for pump wavelength $\lambda_{FF} = 1,550$ nm, versus θ and ϕ, for a p-polarized (panel b) and s-polarized (panel c) pump. (d) Measured SHG efficiency versus θ, for pump wavelength $\lambda_{FF} = 1,550$ nm and $\phi = 45°$. (e) Measured SHG efficiency versus pump wavelength for $\theta = 40°$, $\phi = 45°$ and p-polarized pump.

its zincblende crystal structure, the nonlinear susceptibility tensor of GaAs obeys $t^{-1}\chi^{(2)} \equiv \chi^{(2)}_{xyz} = \chi^{(2)}_{yxz} = \chi^{(2)}_{zxy} = \chi^{(2)}_{xzy} = \chi^{(2)}_{yxz} = \chi^{(2)}_{zyz} \neq 0$, while all the other components vanish [31].

Using the Green's function approach [24], [33], we can retrieve the relationship between the transverse part of the second-harmonic (SH) field and the transverse part of the FF field. The SH field, evaluated at the sheet position, reads

$$E_x^{2\omega} = -\chi^{(2)}\left[2E_y^{\omega}\frac{\partial E_x^{\omega}}{\partial x} + E_y^{\omega}\frac{\partial E_y^{\omega}}{\partial y} + E_x^{\omega}\frac{\partial E_y^{\omega}}{\partial x}\right], \tag{5}$$

$$E_y^{2\omega} = -\chi^{(2)}\left[2E_x^{\omega}\frac{\partial E_y^{\omega}}{\partial y} + E_x^{\omega}\frac{\partial E_x^{\omega}}{\partial x} + E_y^{\omega}\frac{\partial E_x^{\omega}}{\partial y}\right]. \tag{6}$$

The expressions in Eqs. (5) and (6), derived in the Methods, unveil the nonlinear edge detection operation of the NN film. All the terms in the SH fields are proportional to the first-order spatial derivatives of the pump signal multiplied by a component of the signal itself, confirming the nonlinear high-pass filtering operation illustrated in the previous section. An interesting feature of the nonlinear edge detection operation is the role of the polarization state of the pump, which may be used as a control knob to highlight selectively edges with different orientation. To show this, let us first assume that the pump signal is linearly polarized along x, so that the transverse FF signal is $\mathbf{E}_{\perp}^{\omega} = E_x^{\omega}(x, y)\hat{x}$. Since $E_y^{\omega} = 0$, from Eqs. (5) and (6), it follows that the resulting SH field is y-polarized and equal to $E_y^{2\omega} = -\chi^{(2)}E_x^{\omega}\frac{\partial E_x^{\omega}}{\partial x}$. Therefore, large SH signals will be generated by features of the input image with nonzero values of the spatial derivative $\frac{\partial E_x^{\omega}}{\partial x}$; such scenario is obtained, for example, when the input image contains edges that are parallel to y. Instead, edges that are parallel to x will lead to nonzero values of only the derivative $\frac{\partial E_x^{\omega}}{\partial y}$, which in this case does not contribute to the SHG efficiency. Conversely, when the pump signal is y-polarized, the SH field is x-polarized and equal to $E_x^{2\omega} = -\chi^{(2)}E_y^{\omega}\frac{\partial E_y^{\omega}}{\partial y}$. In this scenario, only horizontal edges (parallel to x) will give rise to high SH signals. For circular polarization $\mathbf{E}_{\perp}^{\omega} = E_0(x, y)(\hat{x} \pm i\hat{y})/\sqrt{2}$, with the plus (minus) sign indicating right (left) handedness, the SH field is

$$E_x^{2\omega} = -\frac{1}{\sqrt{2}}\chi^{(2)}\left[\pm 3iE_0\frac{\partial E_0}{\partial x} - E_0\frac{\partial E_0}{\partial y}\right], \tag{7}$$

$$E_y^{2\omega} = -\frac{1}{\sqrt{2}}\chi^{(2)}\left[\pm 3iE_0\frac{\partial E_0}{\partial y} + E_0\frac{\partial E_0}{\partial x}\right]. \tag{8}$$

Therefore, all edges of the FF image are uniformly detected in the generated output image. It is important to emphasize once again the relevant differences between the results obtained here and the edge detection obtained in linear metasurfaces by engineering dispersive optical modes. First, the nonlinear spatial differentiation in Eqs. (7) and (8) (i.e., under circularly polarized pump) is isotropic with respect to azimuthal rotations of the input image – i.e., if the input image is rotated within the xy plane, the output image will be rotated as well, without any image distortion (see also Supplementary Information, Section S4). By contrast, edge detection obtained via Fourier filtering in linear metasurfaces often suffers from poor isotropy [10], [12], due to the fact that a metasurface made of periodic patterns cannot be invariant under arbitrary rotations. The most isotropic responses are obtained with metasurfaces with C_6 rotational symmetry [14], within moderately large ranges of impinging polar angles. Yet, high anisotropies are inevitable for larger impinging angles [14]. Second, the output fields in Eqs. (5)–(8) are proportional to the first-order derivative of the input field. First-order (or, in general, odd-order) differentiation is challenging to achieve in linear patterned metasurfaces, because it requires a unit cell that simultaneously breaks vertical and horizontal symmetry [5], introducing significant fabrication challenges. Instead, the proposed NN thin film provides first-order differentiation naturally, without requiring any symmetry breaking and challenging fabrication processes. Finally, while in the experimental results discussed later the practical effect of the mathematical operations in Eqs. (5)–(8) is to enhance the image edges, the underlying mathematical operation is very different from the linear differential operations demonstrated with linear meta-optic devices [6]–[21]. Here, we induce a nonlinear operation (multiplication of an image by its gradient), which is not achievable with any linear device.

We experimentally demonstrate this nonlinear image processing operation based on the sample shown in Figure 3a, consisting of a 480-nm-thick flat slab of (001) GaAs bonded on a thick quartz substrate. To verify the capability of this thin, unpatterned slab to provide the desired nonlinear image processing operation, we first measured how the SHG efficiency depends on the pump direction, polarization, and wavelength. The sample was illuminated with a quasi-plane-wave pump excitation at the fundamental frequency (wavelength $\lambda_{\text{FF}} \in [1,400, 1,750]$ nm), provided by a tunable pulsed laser (pulse duration 2 ps, repetition rate 80 MHz). The generated SH signal was collected along the same direction as the pump (see Methods for details on the setup). No polarization selection was performed on the collected SH signal. In Figure 3b and c, we show the measured SHG efficiency as a function of the polar (θ) and azimuthal (ϕ) angles of the pump direction (see Figure 3a for the definition of the angles), for a fixed pump wavelength $\lambda_{\text{FF}} = 1,550$ nm and for p-polarization (Figure 3b) and s-polarization (Figure 3c) (see Section 4 for additional details on the measurement protocol). The measured efficiency follows the expected patterns for both polarizations (see Supplementary Information, Section S3, for a comparison between these experiments and numerically calculated data). Figure 3d shows a sliced 1D data for $\phi =$ 45° for both polarizations. The measurements confirm that pumps propagating at normal incidence ($\theta = 0°$) – which in the imaging experiment carry the information on the DC components of the input image – do not lead to any SH generation. As the excitation polar angle θ increases, the SH signal increases monotonically. For s polarization, no SH emission is observed when $\phi = n\pi/2$, as expected from the symmetry of the $\chi^{(2)}$ tensor. For p-polarization, instead, the SH emission is nonzero for any azimuthal angle, albeit with some large modulation.

Importantly, the SHG efficiency depends weakly on the pump wavelength, as shown in Figure 3e. Here, we measured the SHG efficiency versus pump wavelength for fixed $\theta = 40°$, $\phi = 45°$ and p-polarized pump. The SHG efficiency remains above 50 % of its peak value for any $\lambda_{\mathrm{FF}} \in [1,400, 1,750]$ nm. The weak modulation of SHG efficiency as a function of the pump wavelength is due to a combination of the frequency dependence of the $\chi^{(2)}$ of GaAs [34], [35] and the weak Fabry–Perot resonances created by the finite slab, as confirmed by numerical simulations (see Supplementary Information). The decrease in efficiency for $\lambda_{\mathrm{FF}} < 1,450$ nm is attributed to the onset of absorption of the corresponding SH signal in GaAs. In the Supplementary Information (Section S3), we show numerically calculated data corresponding to the measurements in Figure 3b–d, which display excellent agreement with the experiments.

After having verified that our sample can provide the expected nonlinear transfer function, we tested its behavior as a flat optics for nonlinear image processing by using the setup schematized in Figure 4 and discussed in more detail in the Methods. The pump signal was provided by the same tunable pulsed laser used for the measurements in Figure 3. The power and polarization states of the pump were controlled by a series of polarization optics. The collimated laser was then used to illuminate a mask (labeled “target” in Figure 4), which contains different test images. The typical average power on the target was of the order of 1 W, corresponding to a pulse energy of the order of ~10 nJ. The image created by the target was relayed onto the GaAs slab with a projection system (red-shaded box) formed by the lens L_p and the objective O_p (20×, NA = 0.4). The projection system shrinks the image size by a factor of approximately 10×, thus increasing the local pump intensity. A long pass filter (LPF) inside the projection system rejected any SH signal generated by the material forming the mask. The image at the fundamental frequency impinged on the GaAs slab from one side, and the signal emerging from the other side of the slab (containing both the FF and the SH images) was collected by another objective (O_c, 50×, NA = 0.42). This signal was then redirected either to a NIR camera to record the FF image or to a visible camera to record the SH image. In the second case, the strong FF signal was filtered out by two short-pass filters (SPFs). In this experiment, the GaAs slab was oriented such that the [110] direction of GaAs was parallel to the y-direction of the lab reference frame (defined in Figure 4), while the [−110] direction of GaAs was parallel to the x-direction defined in Figure 4.

In Figure 5, we show the experimental results with input images at a pump wavelength $\lambda_{\mathrm{FF}} = 1,550$ nm. In this figure, the pump electric field is circularly polarized, which, based on Eqs. (7) and (8), ensures the enhancement of all edges, independently of their orientation. Here and in all following results, the spatial coordinates on the axis of all figures correspond to calibrated spatial dimensions measured in the plane of the GaAs slab. In Figure 5a and b, the input image (Figure 5a) is a circle with a diameter of 100 μm. The corresponding SHG image (Figure 5b) shows

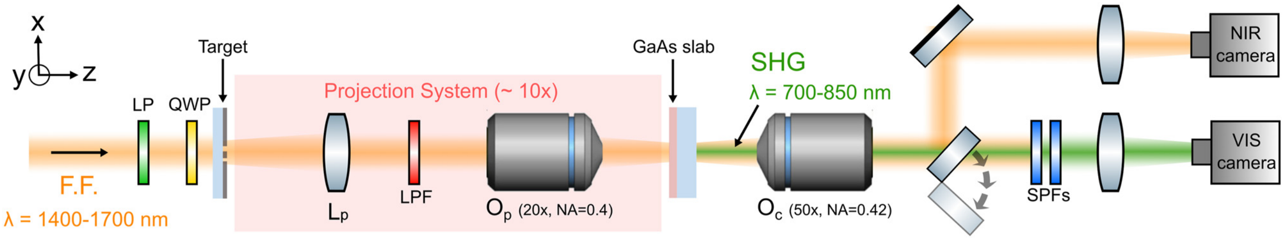

Figure 4: Setup for nonlinear image processing measurements. A pulsed laser with wavelength λ_{FF} is prepared in a certain polarization state and then used to illuminate a mask (“Target”) to create an optical image. A projection system formed by a lens (L_p) and an objective (O_p, 20×, NA = 0.4) relays the image on the GaAs slab. A long pass filter (LPF) inside the projection system rejects any SH signal generated by the target material. The signal propagating on the other side of the GaAs slab (which contains both the FF and the SHG image) is collected by a second objective (O_c, 50×, NA = 0.42) and redirected either to a near-infrared camera or to a visible camera. LP = linear polarizer, QWP = quarter wave plate, LPF = long pass filter, SPFs = short pass filters.

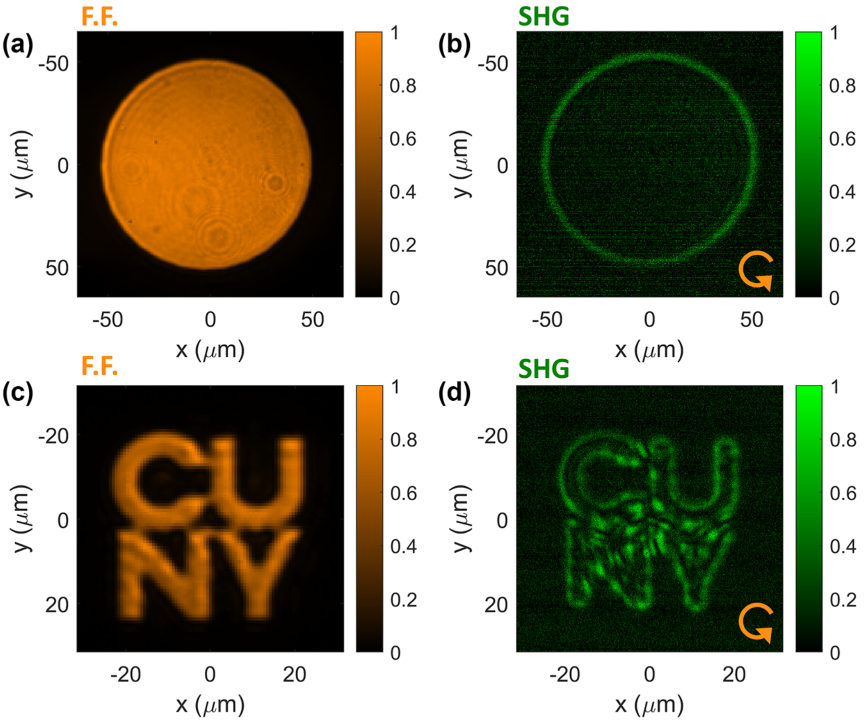

Figure 5: Experimental nonlinear image processing. Nonlinear image processing of different input images carried by a circularly polarized pump with $\lambda_{FF} = 1,550$ nm. (a–b) The input image (panel a) is a circle with a diameter of approximately 100 μm. The image recorded at the SH wavelength (panel b) displays the expected signal processing, i.e., an isotropic enhancement of the edges. (c–d) Same as in panels a–b, but with an input image made of the logo of one of our institutions.

the expected edge-detection functionality: the SH signal is strongly enhanced along the edges of the input images, while it is almost zero in the spatial regions where the intensity of the input image is constant. Similar results are obtained with a different input image, consisting of the logo of one of our institutions (Figure 5c and d).

Next, we investigate the dependence of the features of the output image on the polarization of the input image. To this aim, we consider input images with well-defined edge orientations, such as squares and rectangles. In Figure 6a–e, we consider a fixed input FF image formed by a square with a width of about 50 μm (Figure 6a). We recorded the generated SH image for different input polarizations: horizontal (Figure 6b), vertical (Figure 6c), right circularly polarized (Figure 6d), and left circularly polarized (Figure 6e). As expected from the discussion above, when the input signal is linearly polarized (Figure 6b and c), the edges of the input image that are oriented orthogonal to the input polarization are maximally enhanced in the output images, while edges that are parallel to the input polarization are absent in the output images. Instead, when using circular polarization (with either chirality), all edges are uniformly enhanced (Figure 6d and e). The results in Figure 6a–e were obtained with a “positive” image, i.e., a shape whose internal area has a large intensity, while the external area has zero intensity. We have also verified that the same image processing and polarization-dependent behavior is obtained with “negative” images, i.e., images composed of dark shapes surrounded by a high-intensity background (Figure 6f–j).

Finally, we show that our sample can perform nonlinear image processing over an extremely broad range of input frequencies. In Figure 7, we used the same input image as in Figure 6f–j, and we fixed the input polarization to circular. We varied the input wavelength from $\lambda_{FF} = 1,420$ nm to $\lambda_{FF} = 1,680$ nm and recorded the corresponding SH output images. As shown by the different panels in Figure 7, all output images display well-defined edge detection. The output image is essentially independent of the FF wavelength (indicated in the bottom-right corner of each panel of Figure 7). To quantitatively compare the output intensities and the edge detection efficiency at different input wavelengths, all SHG images in Figure 7 were acquired in the same experimental conditions, and the pixel intensities of each measurement have been normalized by the square of the corresponding FF power. Furthermore, to aid the comparison between different measurements, we normalized all data with respect

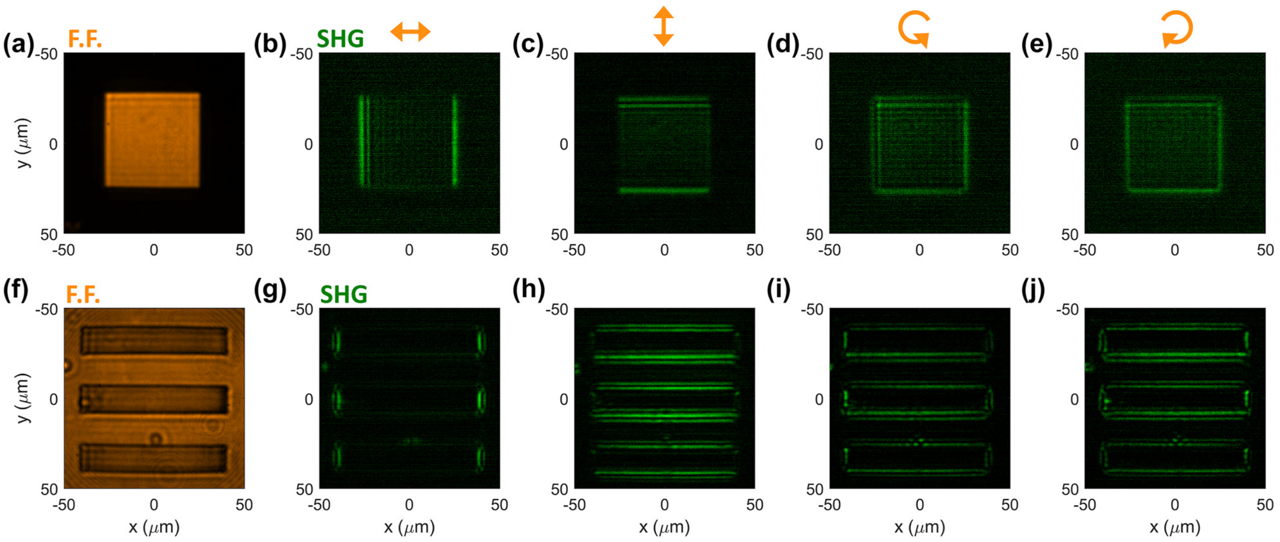

Figure 6: Dependence on input polarization of nonlinear image processing. (a–e) An input image (panel a) containing a "positive" square (i.e., high intensity inside the square) is processed by the GaAs slab. We recorded the generated SH image for different polarization of the input image: horizontal (panel b), vertical (panel c), right circularly polarized (panel d), and left circularly polarized (panel e). (f–j) Same as in panels (a–e), but for the case in which the input image consists of three "negative" rectangles (i.e., zero intensity inside the rectangles).

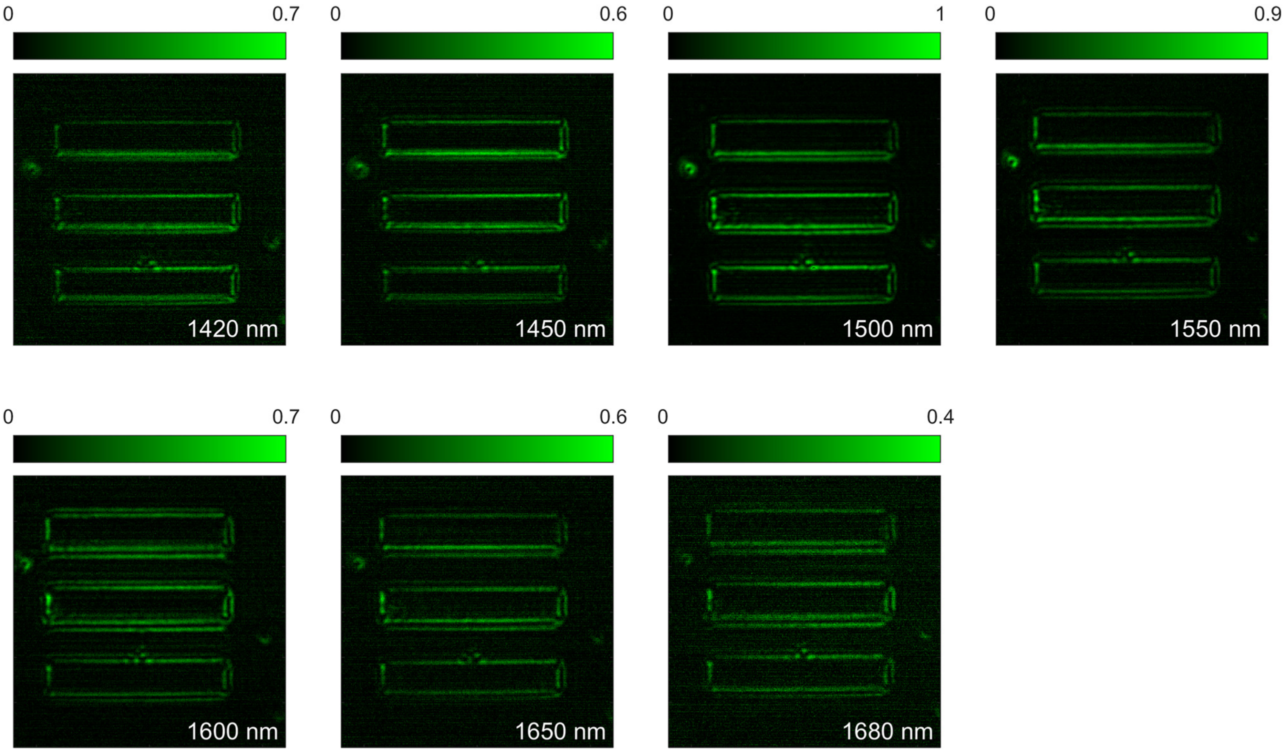

Figure 7: Nonlinear image processing versus input wavelength. The input image is the same as in Figure 5f, and the input polarization is circular. The seven panels in the figure show the recorded SHG image as the input wavelength was varied between 1,420 nm and 1,680 nm. The input wavelength is denoted in the left-bottom corner of each panel. In each measurement, the intensity recorded by the camera was normalized by the squared of the input power. Then, all data were further normalized with the respect to the maximum peak intensity, which occurs for $\lambda_{\mathrm{FF}} = 1,500$ nm.

to the highest peak intensity among all panels in Figure 7. With this procedure, the intensities of the different output images in Figure 7 can be readily compared by looking at the upper bound of the corresponding colorbar. As expected from the efficiency curve in Figure 3e, the highest peak intensity in Figure 7 occurs for $\lambda_{\mathrm{FF}} = 1,500$ nm. Moreover, the variation of the peak intensity with input wavelength is fairly weak, and the peak intensity remains above

0.7 for $\lambda_{\mathrm{FF}} = 1,420$ nm and above 0.4 for $\lambda_{\mathrm{FF}} = 1,680$ nm. We note that the wavelength range considered in Figure 7 (1,420 nm–1,680 nm) was solely determined by the power available in our laser system, and we expect the operational bandwidth to be even larger, ultimately limited only by the increased absorption of the SH within the GaAs slab as the SH wavelength $\lambda_{\mathrm{FF}}/2$ further decreases. In the Supplementary Information (Sections S1–S3), we discuss additional numerical calculations of the SHG efficiency of our GaAs slab versus pump wavelength.

3 Discussion and outlook

In this work, we have proposed and experimentally demonstrated that, by combining nonlinearities with nonlocalities in unpatterned thin films, it is possible to perform analog nonlinear image processing tasks, unlocking fundamental operations and practical metrics of interest that are not available in linear patterned metasurfaces. Based on these principles, we have provided an experimental demonstration of broadband, high-resolution nonlinear edge detection with a thin slab of gallium arsenide, obtained by imparting a nonlinear mathematical operation on the input image.

From a fundamental standpoint, our approach allows performing nonlinear image processing operations – such as the product of the input image by its own derivative. Such operation cannot be implemented in linear devices based on Fourier optics, and it can provide an effective scheme for phase-imaging based on which rapid phase changes are emphasized on top of an existing image. Remarkably, this operation is obtained within a thin unpatterned film, without the need of any nanostructuring, in strong contrast to linear devices which require nanoscale patterning to induce the required k-space transfer function. Here, we instead leverage the inherent nonlocality of an anisotropic thin film. Besides the fundamental difference in working principle and achievable computational tasks, our approach also boosts several key-metrics compared to Fourier-based linear metasurface approaches. Indeed, since our approach does not rely on optical resonances, it is inherently broadband. In our experiment, we demonstrated nonlinear edge detection over a 260 nm bandwidth, only limited by the practical constraints of our setup. Besides the increased spectral bandwidth, the absence of any resonant effect also has other important benefits. First, a nonresonant optical response lifts any strong constraint on the numerical aperture of our device, overcoming typical challenges which instead affect patterned linear metasurfaces that rely on dispersive resonances [14]. Second, the absence of resonant effects largely benefits the power handling capability of our flat device as compared to resonant nonlinear metasurfaces. Indeed, metasurfaces made out of subwavelength resonators typically lead to a resonantly enhanced electric field inside the resonators, which increases the thermal damage induced by free-carrier injection and thus strongly lowers the damage threshold [27]. Instead, our device is completely homogeneous within the in-plane dimensions, thus avoiding any local enhancement of the electric field intensity. This feature dramatically increases the power damage threshold, making it comparable to the one of a bulk crystal. While we trade these advantages for power efficiency – as nonlinear optical processes in thin films are very weak – the SH fields are dominated by the processed image; hence, they can be easily resolved even without strong output power levels. For the implementation of these devices within practical computational applications, it is crucial to boost the power efficiency while retaining a large fidelity of the desired mathematical operation and maintaining large enough spectral bandwidths. This can be achieved by adding weak resonant modes, with low quality factors, to our platform, for example via patterning or by adding thin flat mirrors.

We find these results to fit well in the special issue in honor of Prof. Capasso, whose contributions to nanophotonics, nonlinear and flatland optics have opened the vistas inspiring this work. The phenomena demonstrated in this paper pave the way for the use of flat-optics for nonlinear analog computation, with potential applications in neuromorphic computing, optics-based neural networks, and nonlinear signal processing. In this work, we focused on a flat unpatterned layer, where the nonlinear transfer function $T_{\mathrm{NN}}(\mathbf{k}, \mathbf{k}')$ is solely dictated by the anisotropy of the $\chi^{(2)}$ tensor. We envision that this approach can be extended to nonlinear patterned metasurfaces, whereby the nonlinear transfer function can be further tailored by optical resonances to achieve more advanced nonlinear optical functionalities that would not be accessible within bulk Fourier optics.

4 Methods

4.1 Second-harmonic generation from a thin sheet of GaAs

The nonlinear thin film is modeled as a flat-optics element, or sheet, with quadratic nonlinearity. The sheet is located at $z = 0$. Second-harmonic light emission from the sheet is due to of the interaction of its nonlinear susceptibility with the fundamental-frequency field (or pump field) at $z = 0$.

Let's analyze the quadratic nonlinear response associated with an arbitrary $\chi^{(2)}_{\ell mn}$ element, where ℓ, m, and n indicate Cartesian coordinates. In the Fourier-space representation, the **k**-spectrum of the input pump field (at frequency ω) in the plane of the sheet ($z = 0$) is expressed as a two-dimensional Fourier transform, $\widetilde{E}_i^{\omega}(\mathbf{k}_\perp, 0) = \Im\left[E_i^{\omega}(\mathbf{r}_\perp, 0)\right]$, where $i = x, y, z$, $\mathbf{r}_\perp = (x, y)$ is the direct space in-plane coordinate and $\mathbf{k}_\perp = (k_x, k_y)$ is the spatial-frequency in-plane vector. If the nonlinear susceptibility $\chi^{(2)}_{\ell mn}$ does not introduce angular dispersion, the **k**-spectrum of the second-harmonic field (at frequency 2ω) at any longitudinal position z can be calculated as a convolution of the pump signal field components [24], [33], which in Cartesian coordinates is written as

$$\widetilde{E}_i^{2\omega}(\mathbf{k}_\perp, z^\pm) = \widetilde{G}_{i\ell}(\mathbf{k}_\perp, z^\pm)\,\chi^{(2)}_{\ell mn}\widetilde{E}_m^{\omega}(\mathbf{k}_\perp, 0) * \widetilde{E}_n^{\omega}(\mathbf{k}_\perp, 0), \tag{M1}$$

where the star symbol is the convolution operator and

$$\widetilde{\mathbf{G}}(\mathbf{k}_\perp, z^\pm) = \frac{ie^{\pm ik_z z}}{2k_z}\begin{pmatrix} \dfrac{k_y^2k^2 + k_x^2k_z^2}{k_x^2 + k_y^2} & \dfrac{k_xk_yk_z^2 - k_xk_yk^2}{k_x^2 + k_y^2} & \mp k_xk_z \\ \dfrac{k_xk_yk_z^2 - k_xk_yk^2}{k_x^2 + k_y^2} & \dfrac{k_x^2k^2 + k_y^2k_z^2}{k_x^2 + k_y^2} & \mp k_yk_z \\ \mp k_xk_z & \mp k_yk_z & k_x^2 + k_y^2 \end{pmatrix} \tag{M2}$$

indicates the spectral Green's function. Here, $k_z = \sqrt{k^2 - k_x^2 - k_y^2}$ is the longitudinal component of the wavevector and k is the wavenumber. If the pump signal has a small spatial-frequency spectrum in the transverse plane (corresponding to an input image with features much larger than the free-space wavelength), then $k_z \approx k$ and the expression in Eq. (M1) simplifies to

$$\widetilde{E}_i^{2\omega}(\mathbf{k}_\perp, z^\pm) = \frac{ie^{\pm jkz}}{2k}\begin{pmatrix} k^2 & 0 & \mp k_xk \\ 0 & k^2 & \mp k_yk \\ \mp k_xk & \mp k_yk & k_x^2 + k_y^2 \end{pmatrix} \times \chi^{(2)}_{\ell mn}\widetilde{E}_m^{\omega}(\mathbf{k}_\perp, 0) * \widetilde{E}_n^{\omega}(\mathbf{k}_\perp, 0). \tag{M3}$$

In the case of GaAs, the only nonzero $\chi^{(2)}_{\ell mn}$ elements are those for which $\ell \neq m \neq n$, namely $t^{-1}\chi^{(2)} \equiv \chi^{(2)}_{xyz} = \chi^{(2)}_{yxz} = \chi^{(2)}_{zxy} = \chi^{(2)}_{xzy} = \chi^{(2)}_{yxz} = \chi^{(2)}_{zyz}$,where $t \ll \lambda_0$ is the thickness of the flat-optics element. Therefore, the transverse components of the transmitted second-harmonic field can be written in Fourier space as:

$$\widetilde{E}_x^{2\omega}(\mathbf{k}_\perp, z^\pm) = i\chi^{(2)}ke^{jkz}\Big(\widetilde{E}_y^{\omega}(\mathbf{k}_\perp, 0) * \widetilde{E}_z^{\omega}(\mathbf{k}_\perp, 0) - \frac{k_x}{k}\widetilde{E}_x^{\omega}(\mathbf{k}_\perp, 0) * \widetilde{E}_y^{\omega}(\mathbf{k}_\perp, 0)\Big), \tag{M4}$$

$$\widetilde{E}_y^{2\omega}(\mathbf{k}_\perp, z^\pm) = i\chi^{(2)}ke^{jkz}\Big(\widetilde{E}_x^{\omega}(\mathbf{k}_\perp, 0) * \widetilde{E}_z^{\omega}(\mathbf{k}_\perp, 0) - \frac{k_y}{k}\widetilde{E}_x^{\omega}(\mathbf{k}_\perp, 0) * \widetilde{E}_y^{\omega}(\mathbf{k}_\perp, 0)\Big). \tag{M5}$$

The transverse components of the second-harmonic field at $z = 0^+$, i.e., in transmission, can be retrieved by anti-Fourier transforming the expressions in Eqs. (M4) and (M5):

$$E_x^{2\omega}(\mathbf{r}_\perp, 0^+) = i\chi^{(2)}kE_y^{\omega}(\mathbf{r}_\perp, 0)E_z^{\omega}(\mathbf{r}_\perp, 0) - \chi^{(2)}\frac{\partial\left(E_x^{\omega}(\mathbf{r}_\perp, 0)E_y^{\omega}(\mathbf{r}_\perp, 0)\right)}{\partial x}, \tag{M6}$$

$$E_y^{2\omega}(\mathbf{r}_\perp, 0^+) = i\chi^{(2)}kE_x^{\omega}(\mathbf{r}_\perp, 0)E_z^{\omega}(\mathbf{r}_\perp, 0) - \chi^{(2)}\frac{\partial\left(E_x^{\omega}(\mathbf{r}_\perp, 0)E_y^{\omega}(\mathbf{r}_\perp, 0)\right)}{\partial y}, \tag{M7}$$

where the anti-transformations $ik_x \to \partial/\partial x$ and $ik_y \to \partial/\partial y$ have been applied. Introducing the expression of the longitudinal field as a function of the derivative of the transverse field, $E_z^{\omega} \approx \frac{i}{k}\left(\frac{\partial E_x^{\omega}}{\partial x} + \frac{\partial E_y^{\omega}}{\partial y}\right)$, in Eqs. (M6) and (M7) leads to the expressions reported in Eqs. (5)–(8).

4.2 Sample fabrication

A 480-nm-thick GaAs layer was epitaxially grown on a (001)-oriented GaAs wafer with stop-etch layers. The stop-etch layers consist of 120-nm-thick Al0.55Ga0.45As, 100-nm-thick GaAs, and 20-nm-thick Al0.55Ga0.45As layers, in that order. The wafer was diced to be 10 × 10 mm and flip-chip bonded onto a quartz substrate using epoxy (353ND, EPO-TEK). Then, the GaAs wafer was thinned to be ~20 μm using a mechanical lapping process and removed by a wet-etching process using citric acid etchant (citric acid:H2O2 = 5:1) until the wet etch stops at the Al0.55Ga0.45As stop-etch layer. The stop-etch layers were then wet-etched using a phosphoric acid etchant (H3PO4:H2O:H2O2 = 20:200:4), and the GaAs spacer between them was etched using citric acid etchant. Finally, only the 480-nm-thick GaAs layer remained on the quartz substrate.

4.3 Optical measurements

The measurements shown in Figure 3 were performed with a custom-built setup, shown in Figure 8. The pump signal at the FF, ranging between 1,400 nm and 1,750 nm, was a pulsed laser (pulse duration $\tau = 2$ ps, repetition rate $f = 80$ MHz) provided by the signal of an optical parametric oscillator (APE, Levante IR ps) pumped by an Yb laser (APE,

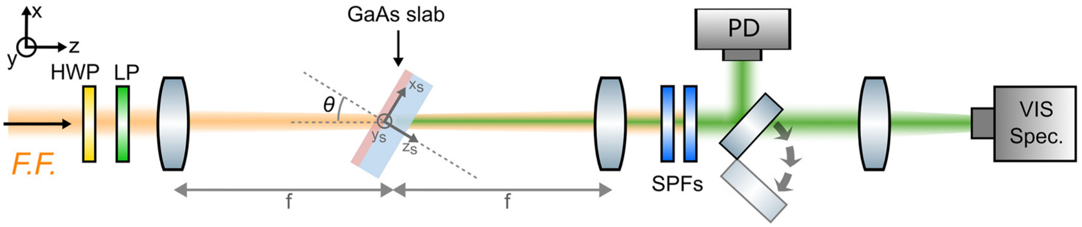

Figure 8: Setup used for preliminary measurements shown in Figure 3. See text for details.

Emerald Engine). The power and polarization of the pump laser were controlled by a half-wave plate (HWP) and a linear polarizer (LP) cascaded in sequence. In all measurements in Figure 3, the average power was kept fixed to about 400 mW (for all impinging angles and all wavelengths), corresponding to a pulse energy of about 5 nJ. The laser was then focused on the sample (from the quartz side) with a long-focal-length lens (focal length = 20 cm), resulting in a spot radius (defined as the distance from the center at which the intensity drops by a factor e^2) of approximately 90 μm. The signal emerging from the opposite side of the sample (containing both the FF and the SH signal) was collected by a second identical lens and recollimated. After removing the FF with a pair of short-pass filters (SPF), the SH signal was redirected either to a visible spectrometer (Ocean Optics, HR4000) or to a photodiode (Thorlabs, DET100A2). The power of the laser (before exciting the sample) was continuously monitored by an additional germanium photodiode (not shown in Figure 8).

To excite the sample with a pump with a well-defined s or p-polarization, we utilized the configuration shown in Figure 8. The reference frame of the lab (labeled as x, y, z, black arrows in Figure 8) is defined such that z is along the optical axis of the setup, and x and y correspond to the *horizontal* and *vertical* polarizations, which can be imparted by LP. We also introduce the reference frame of the sample (x_s, y_s, z_s, gray arrows), shown also in Figure 3, defined such that z_s is always perpendicular to the GaAs layer. The sample was mounted on two different rotation stages: a motorized one (Thorlabs, HDR50) to control the polar angle θ, defined as the angle between the optical axis (z) and z_s (see Figure 8); a manual rotation stage to control the azimuthal angle ϕ, defined as the in-plane rotation of the sample around the axis z_s (see also Figure 3a). The rotational geometry (Figure 8) is chosen such that, when $\theta = 0$ and $\phi = 0$, the reference frames of the lab (x, y, z) and of the sample (x_s, y_s, z_s) coincide (apart from a trivial translation). Moreover, for any value of θ and ϕ, the vertical direction of the lab reference frame (y) is always parallel to the sample plane. Figure 8 shows the particular case of $\phi = 0$, for which the directions y and y_s coincide. Thanks to this configuration, when the pump is polarized along the y direction of the lab frame (*vertical* polarization), the electric field of the pump always lies in the sample plane, for any value of θ and ϕ. This corresponds to s polarization. Conversely, when the pump is polarized along the x direction of the lab frame (horizontal polarization), the magnetic field of the pump is along y, and thus it will always lie in the sample plane, for any value of θ and ϕ. This corresponds to p polarization.

The measurements in Figure 3b–d were performed by keeping the FF wavelength fixed at $\lambda_{\mathrm{FF}} = 1,550$ nm and by continuously varying the angles θ and ϕ of the sample while acquiring the SHG spectra with the spectrometer. The signal recorded by the spectrometer in a narrow region around $\lambda_{\mathrm{FF}}/2$ was then used to retrieve the SHG efficiency. The procedure was repeated for two different orientations of the linear polarizer (LP), in order to set the pump polarization to either s or p as described above. The measurements in Figure 3e were performed by varying the pump wavelength in the 1,400 nm–1,750 nm range while keeping all other parameters fixed. The SHG signal produced by each pump was recorded by the photodiode, and the SHG efficiency (in arbitrary units) was obtained by dividing the voltage read by the photodiode by the square of the laser power (measured separately for each wavelength). The wavelength dependence of the photodiode efficiency (provided by the vendor) was used to correct the measured voltages.

The measurements in Figures 5–7 were acquired with the setup shown in Figure 4 and described in the main text. The laser source was the same as in the setup described in the previous paragraph.

Research funding: Air Force Office of Scientific Research MURI program; Simons Foundation. Ministero dell'Istruzione e del Merito (METEOR, PRIN-2020 2020EY2LJT_002); H2020 Future and Emerging Technologies (FETOPEN-2018-2020 899673, METAFAST). Australian Research Council Centres of Excellence Program (CE200100010). IB and HJ acknowledge support from the U.S. Department of Energy, Office of Basic Energy Sciences, Division of Materials Sciences and Engineering. This work was performed in part at the Center for Integrated Nanotechnologies, an Office of Science User Facility operated for the US Department of Energy (DOE) Office of Science. Sandia National Laboratories is a multimission laboratory managed and operated by National Technology and Engineering Solutions of Sandia, LLC, a wholly owned subsidiary of Honeywell International, Inc., for the U.S. Department of Energy's National Nuclear Security Administration under contract DE-NA0003525. This paper describes objective technical results and analysis. Any subjective views or opinions that might be expressed in the paper do not necessarily represent the views of the U.S. Department of Energy or the United States Government.

Author contributions: DdC, CDA, MC, and AA conceived the original idea and designed the experiment. DdC and CDA performed the theoretical analysis and simulations. HJ and IB fabricated the sample. MC built the optical setups, performed the measurements, and analyzed the data. MC, DdC, CDA, and AA wrote the manuscript, with inputs from all authors. All authors have accepted responsibility for the entire content of this manuscript and consented to its submission to the journal, reviewed all the results, and approved the final version of the manuscript.

Conflict of interest: Authors state no conflicts of interest.

Data availability: Data underlying the results presented in this paper may be obtained from the authors upon reasonable request.

References

[1] A. I. Kuznetsov, *et al*., "Roadmap for optical metasurfaces," *ACS Photonics*, vol. 11, no. 3, pp. 816—865, 2024.

[2] A. Overvig and A. Alù, "Diffractive nonlocal metasurfaces," *Laser Photonics Rev.*, vol. 16, no. 8, p. 2100633, 2022.

[3] H. Kwon, D. Sounas, A. Cordaro, A. Polman, and A. Alù, "Nonlocal metasurfaces for optical signal processing," *Phys. Rev. Lett.*, vol. 121, no. 17, p. 173004, 2018.

[4] J. W. Goodman, *Introduction to Fourier Optics*, New York, McGraw-Hill, 1996.

[5] H. Kwon, A. Cordaro, D. Sounas, A. Polman, and A. Alù, "Dual-polarization analog 2D image processing with nonlocal metasurfaces," *ACS Photonics*, vol. 7, no. 7, pp. 1799—1805, 2020.

[6] A. Silva, F. Monticone, G. Castaldi, V. Galdi, A. Alù, and N. Engheta, "Performing mathematical operations with metamaterials," *Science*, vol. 343, no. 6167, pp. 160—163, 2014.

[7] A. Pors, M. G. Nielsen, and S. I. Bozhevolnyi, "Analog computing using reflective plasmonic metasurfaces," *Nano Lett.*, vol. 15, no. 1, pp. 791—797, 2015.

[8] D. A. Bykov, L. L. Doskolovich, E. A. Bezus, and V. A. Soifer, "Optical computation of the Laplace operator using phase-shifted Bragg grating," *Opt. Express*, vol. 22, no. 21, pp. 25084—25092, 2014.

[9] N. V. Golovastikov, D. A. Bykov, L. L. Doskolovich, and E. A. Bezus, "Spatial optical integrator based on phase-shifted Bragg gratings," *Opt. Commun.*, vol. 338, pp. 457—460, 2015.

[10] A. Cordaro, H. Kwon, D. Sounas, A. F. Koenderink, A. Alù, and A. Polman, "High-index dielectric metasurfaces performing mathematical operations," *Nano Lett.*, vol. 19, no. 12, pp. 8418—8423, 2019.

[11] A. Youssefi, F. Zangeneh-Nejad, S. Abdollahramezani, and A. Khavasi, "Analog computing by Brewster effect," *Opt. Lett.*, vol. 41, no. 15, pp. 3467—3470, 2016.

[12] Y. Zhou, H. Zheng, I. I. Kravchenko, and J. Valentine, "Flat optics for image differentiation," *Nat. Photonics*, vol. 14, no. 5, pp. 316—323, 2020.

[13] A. Chizari, S. Abdollahramezani, M. V. Jamali, and J. A. Salehi, "Analog optical computing based on a dielectric meta-reflect array," *Opt. Lett.*, vol. 41, no. 15, pp. 3451—3454, 2016.

[14] M. Cotrufo, A. Arora, S. Singh, and A. Alù, "Dispersion engineered metasurfaces for broadband, high-NA, high-efficiency, dual-polarization analog image processing," *Nat. Commun.*, vol. 14, no. 1, p. 7078, 2023.

[15] A. Saba, M. R. Tavakol, P. Karimi-Khoozani, and A. Khavasi, "Two-dimensional edge detection by guided mode resonant metasurface," *IEEE Photonics Technol. Lett.*, vol. 30, no. 9, pp. 853—856, 2018.

[16] J. Zhou, *et al*., "Optical edge detection based on high-efficiency dielectric metasurface," *Proc. Natl. Acad. Sci.*, vol. 116, no. 23, pp. 11137—11140, 2019.

[17] O. Y. Long, C. Guo, H. Wang, and S. Fan, "Isotropic topological second-order spatial differentiator operating in transmission mode," *Opt. Lett.*, vol. 46, no. 13, pp. 3247—3250, 2021.

[18] T. Zhu, *et al*., "Plasmonic computing of spatial differentiation," *Nat. Commun.*, vol. 8, no. 1, p. 15391, 2017.

[19] A. Komar, R. A. Aoni, L. Xu, M. Rahmani, A. E. Miroshnichenko, and D. N. Neshev, "Edge detection with mie-resonant dielectric metasurfaces," *ACS Photonics*, vol. 8, no. 3, pp. 864—871, 2021.

[20] A. Cordaro, B. Edwards, V. Nikkhah, A. Alù, N. Engheta, and A. Polman, "Solving integral equations in free space with inverse-designed ultrathin optical metagratings," *Nat. Nanotechnol.*, vol. 18, no. 4, pp. 365—372, 2023.

[21] L. Wesemann, J. Rickett, T. J. Davis, and A. Roberts, "Real-time phase imaging with an asymmetric transfer function metasurface," *ACS Photonics*, vol. 9, no. 5, pp. 1803—1807, 2022.

[22] M. Cotrufo and A. Alù, "Metamaterials for analog all-optical computation," *Prog. Opt.*, vol. 69, p. 211, 2024.

[23] R. Kolkowski, T. K. Hakala, A. Shevchenko, and M. J. Huttunen, "Nonlinear nonlocal metasurfaces," *Appl. Phys. Lett.*, vol. 122, no. 16, 2023. https://doi.org/10.1063/5.0140483.

[24] D. de Ceglia, A. Alù, D. N. Neshev, and C. D. Angelis, "Analog image processing with nonlinear nonlocal flat optics," *Opt. Mater. Express*, vol. 14, no. 1, pp. 92—100, 2024.

[25] L. Carletti, A. Locatelli, O. Stepanenko, G. Leo, and C. D. Angelis, "Enhanced second-harmonic generation from magnetic resonance in AlGaAs nanoantennas," *Opt. Express*, vol. 23, no. 20, pp. 26544—26550, 2015.

[26] V. F. Gili, *et al*., "Monolithic AlGaAs second-harmonic nanoantennas," *Opt. Express*, vol. 24, no. 14, pp. 15965—15971, 2016.

[27] S. Liu, *et al*., "Resonantly enhanced second-harmonic generation using III—V semiconductor all-dielectric metasurfaces," *Nano Lett.*, vol. 16, no. 9, pp. 5426—5432, 2016.

[28] R. Camacho-Morales, *et al*., “Nonlinear generation of vector beams from AlGaAs nanoantennas,” *Nano Lett.*, vol. 16, no. 11, pp. 7191–7197, 2016.

[29] R. E. Collin, *Antennas and Radiowave Propagation*, New York, McGraw-Hill, 1985.

[30] J. E. Sipe, V. C. Y. So, M. Fukui, and G. I. Stegeman, “Analysis of second-harmonic generation at metal surfaces,” *Phys. Rev. B*, vol. 21, no. 10, pp. 4389–4402, 1980.

[31] L. Alloatti, *et al*., “Second-order nonlinear optical metamaterials: ABC-type nanolaminates,” *Appl. Phys. Lett.*, vol. 107, no. 12, p. 121903, 2015.

[32] J. Lee, *et al*., “Giant nonlinear response from plasmonic metasurfaces coupled to intersubband transitions,” *Nature*, vol. 511, no. 7507, pp. 65–69, 2014.

[33] J. E. Sipe, “New Green-function formalism for surface optics,” *J. Opt. Soc. Am. B*, vol. 4, no. 4, pp. 481–489, 1987.

[34] D. Bethune, A. Schmidt, and Y. Shen, “Dispersion of nonlinear optical susceptibilities of InAs, InSb, and GaAs in the visible region,” *Phys. Rev. B*, vol. 11, no. 10, p. 3867, 1975.

[35] S. Bergfeld and W. Daum, “Second-harmonic generation in GaAs: experiment versus theoretical predictions of χ x y z (2),” *Phys. Rev. Lett.*, vol. 90, no. 3, p. 036801, 2003.

Supplementary Material: This article contains supplementary material (https://doi.org/10.1515/nanoph-2024-0770).